Laser processing of dielectrics using spatiotemporally tuned ultrashort pulses

Cite as: J. Laser Appl. **32**, 022041 (2020); https://doi.org/10.2351/7.0000081
Submitted: 01 April 2020 . Accepted: 01 April 2020 . Published Online: 30 April 2020

Boyang Zhou, Arifur Rahaman, Xinpeng Du, Aravinda Kar, M. J. Soileau, and Xiaoming Yu

Journal of Laser Applications ARTICLE scitation.org/journal/jla

Laser processing of dielectrics using spatiotemporally tuned ultrashort pulses

Cite as: J. Laser Appl. 32, 022041 (2020); doi: 10.2351/7.0000081
Submitted: 1 April 2020 · Accepted: 1 April 2020 ·
Published Online: 30 April 2020

Boyang Zhou,[1] Arifur Rahaman,[1] Xinpeng Du,[1] Aravinda Kar,[1] M. J. Soileau,[1,2,3] and Xiaoming Yu[1,a)]

AFFILIATIONS

[1]CREOL, The College of Optics and Photonics, University of Central Florida, Orlando, Florida 32816
[2]Department of Physics, University of Central Florida, Orlando, Florida 32816
[3]Department of Electrical and Computer Engineering, University of Central Florida, Orlando, Florida 32816

Note: This paper is part of the Special Collection: Proceedings of the International Congress of Applications of Lasers & Electro-Optics (ICALEO® 2019).

[a)]**Electronic mail:** yux@creol.ucf.edu

ABSTRACT

The authors report on the theoretical and experimental studies of laser-induced optical breakdown on the surface of fused silica to elucidate the influence of time delay and spatial separation between two ultrashort pulses on the position and size of the modification. Carriers involved in the damage formation including free electrons in the conduction band and self-trapped excitons (STEs) are investigated. The relationship between damage morphology and time delay shows that the seeding carriers (free electrons and STEs) generated from the first pulse are found to play a significant role for the second pulse—which is temporally and spatially separated from the first pulse—in creating the critical electron density needed for an optical breakdown. Consequently, processing outcomes, such as accuracy (position of the hole) and resolution (size of the hole), depend on the interplay of various laser-induced physics that can be tailored for specific goals. As a demonstration, laser lithography with resolution below the diffraction limit is achieved by exploiting multipulse induced physics. This work is a step toward repeatable laser processing of dielectrics beyond the diffraction limit and provides insights into ultrafast laser-matter interaction under the condition of an extremely high pulse repetition rate.

Key words: Temporally and spatially separated pulses, self-trapped excitons (STEs), laser lithography below the diffraction limit

I. INTRODUCTION

Minimal thermal effects associated with ultrafast laser ablation have enabled high-precision processing of a wide range of materials including metals, semiconductors, dielectrics, and polymers.[1–4] However, the understanding of the fundamental mechanism involved in ultrafast laser ablation and the exploration of processing methods suitable for industrial use are still incomplete. Two basic physical processes including multiphoton ionization (MPI) and avalanche ionization (AI) are known to be involved in the accumulation of free electron density during the damage formation. A rate-equation model that takes MPI and AI into account has been proposed by Stuart *et al.*[5–7] to describe the change of free electron density (n) during the damage formation. They showed that electrons in the conduction band (CB) generated by AI can achieve the critical plasma density when enough seed electrons are produced by MPI at a peak laser intensity of 12 TW/cm^2 for fused silica. Li *et al.*[8] added an electron decay term n/τ (where τ is the electron decay time) into the rate equation for a more realistic description of an optical breakdown in fused silica. Sudrie *et al.*[9] replaced the MPI term with Keldysh's theory, where the electric field E instead of laser intensity I was considered as the fundamental parameter for photoionization. Wu *et al.*[10] included the maximum valence-band (VB) electron density in the model based on their transmissivity and reflectivity measurements with fused silica. These and other researchers' works show that AI plays a considerable role in the increase of CB free electron density for the damage formation, providing the possibility that precisely controlling free electron density around the critical electron density can achieve novel fabrication results. Joglekar *et al.*[11] verified this possibility by using

1053 nm laser pulse of repetition rate 1.5 kHz and pulse width 800 fs. They were able to generate a laser damage spot of size $43.2 \times 38.4\ \text{nm}^2$ and a scanning channel of width 30.9 nm on glass substrates. In addition, they pointed out that AI should be considered as dominant during the damage formation. However, it remains debatable whether AI plays a significant role in the optical breakdown by femtosecond laser pulses with a shorter pulse duration. Temnov *et al.*[12] found that six-photon ionization is the dominant ionization mechanism in fused silica at the intensity of approximately $10\ \text{TW/cm}^2$ for a laser wavelength of 800 nm. However, achieving nanosized structures by "thresholding" is very sensitive to pulse-to-pulse fluctuation. It is possible to prove that the decrease of free electron density is very sensitive to the decrease of laser intensity when laser intensity is very close to the damage threshold. From this point of view, using single-pulse "thresholding" for below-diffraction-limit lithography has limited repeatability. Englert *et al.*[13] applied asymmetric temporal pulse train to surface processing on fused silica with the size below the diffraction limit. Yu *et al.*[14] reported experimental results of 300 nm feature generated on fused silica using a near-infrared femtosecond laser pulse seeded by an ultraviolet pulse with the consideration of self-trapped excitons (STEs). The significance of STEs was demonstrated in an earlier study by Grojo *et al.*[15]

The present work explores the potential of using temporally and spatially separated laser pulses to generate laser ablation within a size smaller than the diffraction limit on the surface of fused silica. Using computer simulation, the mechanism of femtosecond laser ablation in fused silica including PI (photoionization, including MPI and tunneling ionization), AI, and STEs will be investigated. The purpose is to identify a simple and yet effective model to relate processing parameters with damage size and position. Next, experimental results of laser ablation by using temporally and spatially separated femtosecond laser pulses will be shown to demonstrate the potential of controlling damage size and position by tuning the delay time between two cross-polarized spatially separated pulses.

II. EXPERIMENTAL SETUP

A schematic of the experimental setup is shown in Fig. 1. Laser pulses of duration 167 fs, 1 kHz repetition rate, and 1030 nm center wavelength are provided by a femtosecond laser system (Pharos, Light Conversion). At the laser output, the beam is linearly polarized with the *E*-field parallel to the optical table. The beam is passed through a 50:50 beam splitter (BS1), which splits the beam into two arms (Beam 1 and Beam 2). There is a delay line consisting of two mirrors (M2 and M3) mounted on a linear translation stage (TS) in Beam 2. By moving TS, the delay time (Δt) of the pulses between Beam 1 and Beam 2 is adjusted with a temporal resolution of 0.67 fs. In this experiment, the range of delay time between two pulses is from −1 to 1 ps with a step of 100 fs. The negative delay means that Beam 1 (lower spot in the inset of Fig. 1) arrives at the sample first. The polarization of Beam 1 is turned vertical by a half-wave plate (HWP), so the two beams are cross-polarized to avoid interference. Beam 1 is the vertically polarized beam (VPB) and Beam 2 is the horizontally polarized

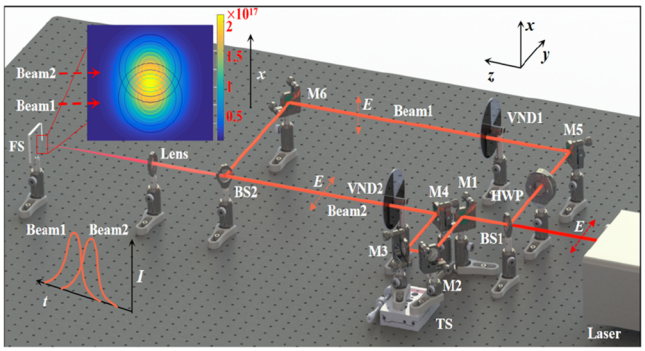

FIG. 1. Experimental setup. BS1 and BS2, beam splitter; HWP, half-wave plate; TS, translation stage; VND1 and VND2, variable-neutral-density filter; M1 to M6, silver mirrors; FS, fused silica sample. Insets show the spatial and temporal relation between two beams as observed on the sample.

beam (HPB). VPB and HPB are focused on the front surface of a fused silica sample by a lens that has a focal length of 300 mm. The spatial separation of two beams is achieved by tuning a mirror (M6) and observing the separation using a camera (not shown) located directly behind the sample. In this experiment, the spatial separation of the two pulses is 20 μm (the $1/e^2$ spot size of each beam is 23 μm). The zero temporal delay is found using the technique of field autocorrelation, by which the delay-dependent interference signal is fitted with a Gaussian function, and $\Delta t = 0$ is determined as the peak of the Gaussian profile. It should be noted that the two beams are copolarized only for determining $\Delta t = 0$. Two variable-neutral-density filters (VND1 and VND2) are used to control the laser powers of Beam 1 and 2, respectively. In this experiment, both beams are kept below the single-shot damage threshold, which is measured as $2.14\ \text{J/cm}^2$. The sample after laser irradiation is examined by a bright-field microscope and phase-contrast microscopy for damage size measurement and surface morphology analysis.

III. MODEL

To understand the formation of laser damage in fused silica by temporally and spatially separated femtosecond laser pulses, a model that consists of the electron density rate equation, the STE rate equation, and Keldysh's equation of photoionization[9] are used as follows:

$$\frac{dn_e}{dt} = (W_{PI} + \eta I n_e)\left(1 - \frac{n_e}{n_{\max}}\right) + \sigma_j I^j n_{STE} - \frac{n_e}{\tau_e}, \tag{1}$$

$$\frac{dn_{STE}}{dt} = \frac{n_e}{\tau_e} - \sigma_j I^j n_{STE} - \frac{n_{STE}}{\tau_{STE}}, \tag{2}$$

$$W_{PI}(|E|) = \frac{2\omega}{9\pi}\left(\frac{\omega m}{\hbar\sqrt{\Gamma}}\right)^{3/2} Q(\gamma, x)\exp(-\alpha\langle x+1\rangle). \tag{3}$$

TABLE I. Parameters used in the simulation.

	Symbol	Description	Value
Constants	m_e	Free electron mass	0.91×10^{-30} kg
	ε_0	Vacuum permittivity	8.854×10^{-12} F/m
	e	Electron charge	1.602×10^{-19} C
	$\hbar$	Planck's constant	1.06×10^{-34} J/s
Laser properties	λ_0	Center wavelength	1030 nm
	ω	Laser frequency	1.83×10^{18} Hz
	w_0	Beam radius at focal point	24 μm
	τ_p	Pulse duration	167 fs
Material properties	U_i	Bandgap	9.0 eV (Ref. 7)
	m	Effective mass of electron	$0.86m_e$ (Ref. 7)
	τ_e	Electron trapping time	150 fs (Ref. 6)
	τ_{STE}	STE decay time	1 ps (Ref. 6)
	η	Avalanche ionization coefficient	4 ± 0.5 cm^2/J
	n_0	Refractive index of fused silica	1.45 (Ref. 7)
	n_i	Initial CB electron density	10^{17} cm^{-3} (Ref. 6)
	σ_j	STE ionization cross section	0.0001 (TW cm^{-2})$^{-6}$ ps^{-1} (Ref. 15)

In this model, the contribution from two types of carriers is included. One is free electron density in CB and the other is STE density accumulated by decayed free electrons. Here, n_e is the free electron density in the conduction band and n_{STE} represents the STE density. The source of free electrons in CB includes the free electrons excited from VB through PI (including MPI and tunneling ionization) and AI processes, and free electrons re-excited from STEs through MPI. The source of STE is the decay of CB free electron, and the initial value of n_{STE} is assumed as 0. As for the PI process, W_{PI} denotes the rate of photoionization. $\gamma = \omega\sqrt{mU_i}/eE$ is the adiabaticity parameter for solids, where $m = 0.635m_e$ is the reduced mass of electrons and holes in solids (m_e is the electron mass). ω is the laser frequency, and U_i is the bandgap of fused silica. $E = \sqrt{2I/n_0\varepsilon_0 c}$ is the amplitude of input electrical field, where n_0 is the refractive index of fused silica, ε_0 is vacuum permittivity, and c is the speed of light in vacuum. Other parameters involved in the calculation of W_{PI} are defined according to Ref. 7 as $\Gamma = \gamma^2/(\gamma^2+1)$, $\Xi = 1-\Gamma$, $Q(\gamma, x) = \sqrt{\pi/2K(\Xi)} \times \sum_{n=0}^{\infty} \exp(-n\alpha)\Phi\left[\sqrt{\beta(n+2\nu)}\right]$, $\alpha = \frac{\pi(K(\Gamma)-E(\Gamma))}{E(\Xi)}$, $\beta = \frac{\pi^2}{4K(\Xi)E(\Xi)}$, $x = \frac{2}{\pi}\frac{U_i}{\hbar\omega}\frac{1}{\sqrt{\Gamma}}E(\Xi)$, and $\nu = \langle x+1\rangle - x$, where $\langle x\rangle$ denotes the integer part of the value x, K and E denote the complete elliptic integral of the first and second kind, respectively, and Φ is the Dawson function $\Phi(z) = \int_0^z \exp(y^2 - z^2)dy$. AI is modeled in the term $\eta I n_e$, where η is the avalanche coefficient and I is the laser intensity. η is adjusted between 4 ± 0.5 cm^2/J to get a good fitting to the experimental data. $I = 2P_{in}/(PRR \cdot \pi w_0^2 \tau_p)$ is the laser intensity, where P_{in} is the input laser power, PRR is the pulse repetition rate, w_0 is the beam radius at the focal point, and τ_p is the pulse duration. n_{max} is the available VB electron density. τ_e is the trapping time of CB electrons and τ_{STE} is the decay rate of STE. We use $j = 6$ for STE ionization cross section σ_j. The decay time of these electrons is 150 fs and all of them are assumed to decay into defect states that have a bandgap of 2 eV. In this work, these three equations are solved simultaneously by means of finite difference to obtain the spatial and temporal dependence of the free electron density. The initial value of n_e is n_{i} at the surface of the sample before the laser pulse arrives. η is the only free parameter in the fitting. The parameters used in the simulation are listed in Table I.

IV. RESULTS AND ANALYSIS

A. Experimental results

The delay time between two pulses is varied from −1 to 1 ps with a step of 100 fs, which is shorter than the pulse duration. It has been shown that the delay has an important effect on free-carrier density distribution in double- and multiple-pulse induced damages.[16,17] However, the delay used in previous studies is typically longer than the pulse duration.[6] By changing the delay in a step less than or comparable to the laser pulse duration, it is possible to observe how the laser properties influence the change of free-carrier density and damage morphology.

As shown in Fig. 2(a), the central position of the damage changes at different delay times. The deviation from the center line [red in Fig. 2(a)] is plotted in Fig. 2(b). The damage center will first deviate from the center of the two beams at shorter delays (<300 fs) and then returns to the original position at longer delays (300 fs to 1 ps).

Figure 3 shows the change of laser damage shape and size measured and simulated at different delay times ranging from −600 to 600 fs with the step of 100 fs. In Figs. 3(a) and 3(b), two-dimensional experimental damages are measured by the bright-field microscope and the phase-contrast microscope, respectively. Each damage spot is measured three times to reduce experimental error. The damage shape changes from elliptical to "tear-drop" shape before 200 fs and then becomes smaller circles after 200 fs. The damage diameter slightly decreases before 200 fs and then sharply decreases after 200 fs.

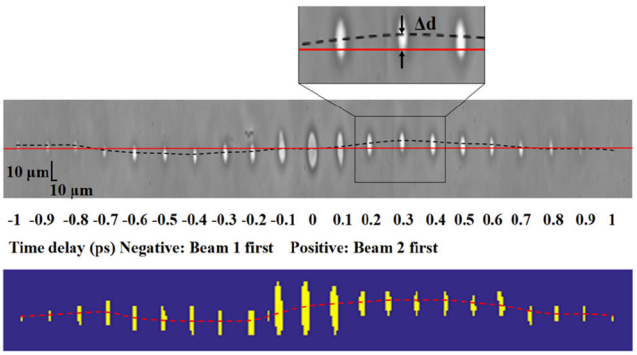

(a)

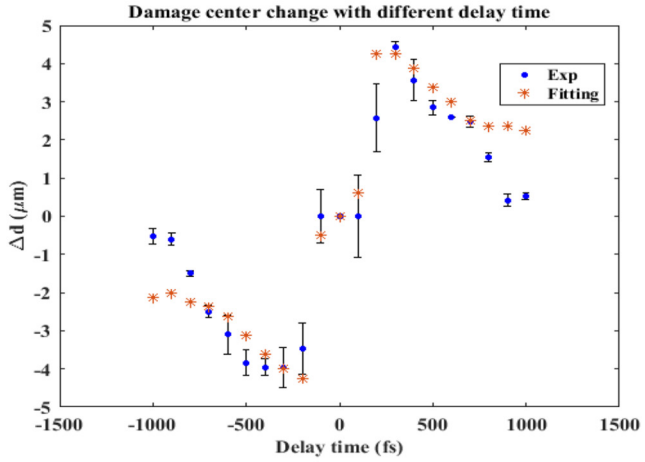

(b)

FIG. 2. Change of damage position with different delays. (a) Phase-contrast image of experimental results (upper figure) and software-processed image (lower figure). (b) Deviation from the center line [red line in (a)] measured as a function of delay. The error bars are plotted at the level of ±1 standard deviation of the mean.

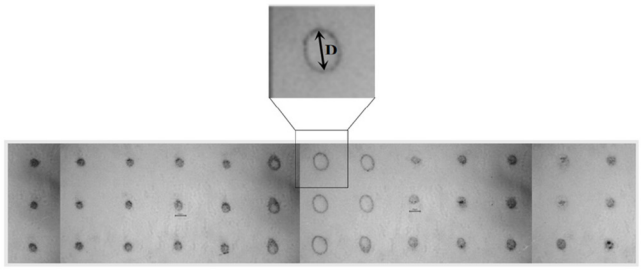

(a)

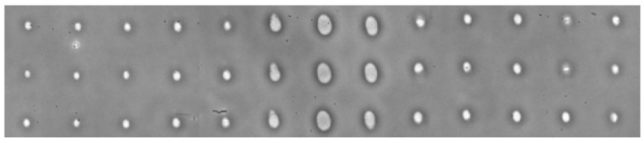

(b)

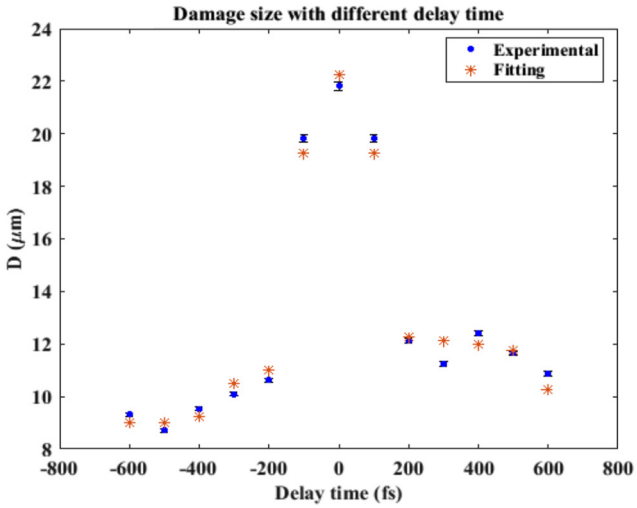

(c)

FIG. 3. Experimental damage morphology and fitting results of different delay times. (a) 2D experimental damage morphology measured by a bright-field microscope. (b) 2D experimental damage morphology measured by a phase-contrast microscope. (c) Experimental and fitting results of damage size. Dots: experimental data. Stars: fitting result. The error bars are plotted at the level of ±1 standard deviation of the mean.

The depth of the damage is measured and shown in Fig. 4. Figure 4(a) shows the depth profile of the damage at different delay times 0, 100, 300, and 600 fs. It is clearly seen that the depth of the damage decreases with increasing delay time. From Fig. 4(b), it can be seen that a sharp decrease of depth occurs when the delay time changes from 0 to 200 fs followed by a slow decrease of depth when delay time is longer than 200 fs, which is very similar to the trend of the damage size at different delay times.

B. Discussion

Figure 2 identifies two key properties of the damage change. First, the damage forms at the place where the first pulse arrives at the sample surface when the delay time is longer than 100 fs. Second, the damage center deviates from the overlapping region of the two beams at first and then returns to the center at a longer delay time. These two properties are due to the change of free electron and STE density distribution at different delay times as shown in Figs. 5(a) and 5(b).

The three pictures of the left column in Fig. 5(a) show how the densities of CB free electron and STE change during the damage formation. When the delay time is zero, the initial free electrons of the substrate are excited by both pulses at the same

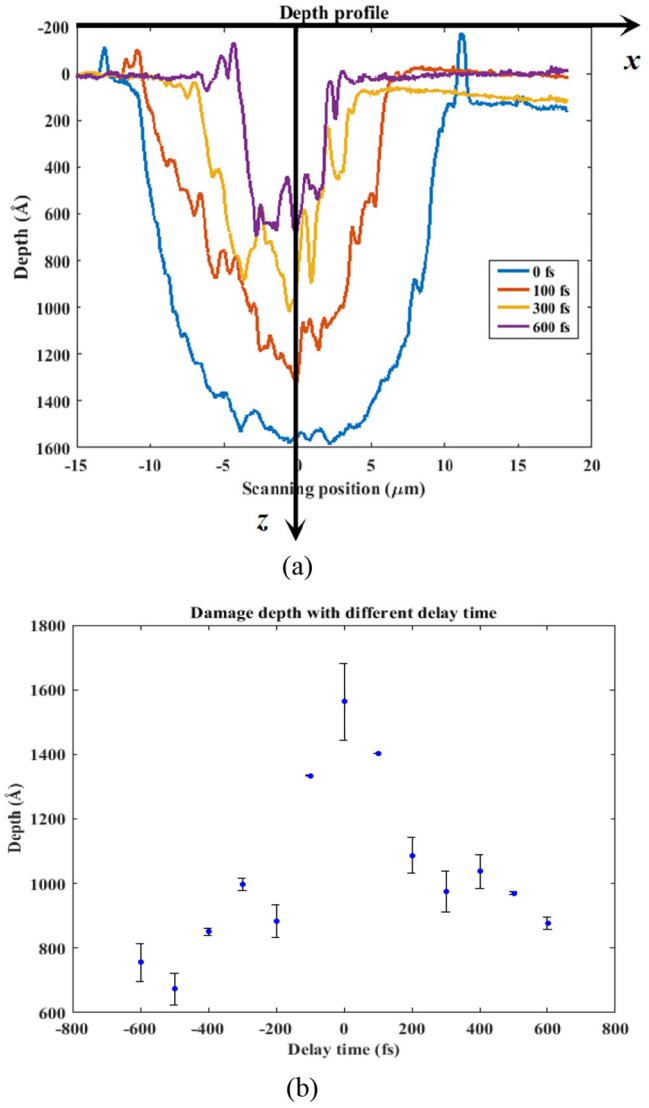

FIG. 4. Damage depth profile and depth change at different delay times. (a) Damage depth profile at different delay times. (b) Maximum depth measured at different delay times. The error bars are plotted at the level of ±1 standard deviation of the mean.

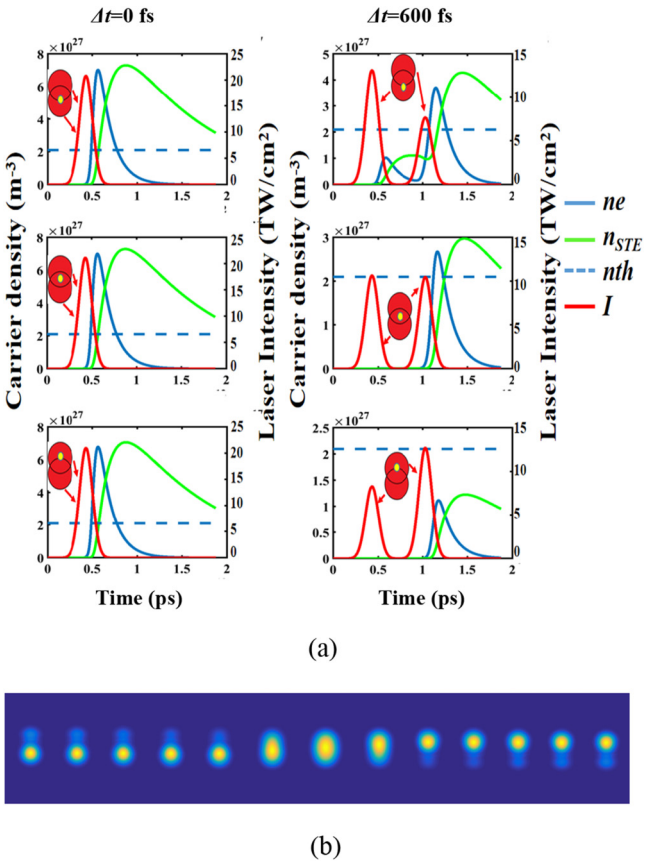

FIG. 5. Simulation results of free-carrier density change at different delay times. (a) Free-carrier density change when delay time is 0 and 600 fs. (b) 2D simulation of the free electron density distribution.

time. The density of free electrons is symmetrically distributed in the areas of the first and second pulses and thus the damage is at the center of the two laser focal areas.

When the delay time is larger than zero but shorter than 150 fs,[14] the latter of which is the decay time of free electron in the conduction band, some of the free electrons, which were originally excited by the first laser pulse, decays to the STE states. The remaining free electrons in the conduction band become the seed electrons for generating new free electrons by the second laser pulse. Compared to the condition of zero delay time, the seed electron density is smaller in the place where the second pulse is incident. Thus, the density of free electron is smaller in the area of the second pulse leading to the damage size is smaller in the area of the second pulse. Though the damage size changes in the area of the second pulse, the damage center is still the same as the condition of zero delay.

The condition becomes complicated when the delay time is longer than 150 fs[14] but shorter than 1 ps,[14] the latter of which is the lifetime of STE. The changes in the CB free electron and STE densities are shown in three figures on the right column in Fig. 5(a). Two cases should be considered in these figures. First, when the delay time is longer than 150 fs but shorter than 400 fs, most of the free electrons excited by the first pulse decay to STE states leaving a small amount of free electrons in CB. Both of the free electrons from STE states and the remaining free electrons excited by the first pulse become the source of seed electrons for the second pulse. Second, when the delay time is equal to or longer than 400 fs, almost all of the free electrons excited by first pulse decay to the STE states. The free electrons ionized from the STE states mainly contribute to the seed electrons for the second

pulse. Spatially, in these two cases, the density of seed electrons for the second pulse is very small in the area of the second pulse leading to a localized damage formation in the area of the first pulse. Thus, the damage forms at the place where the first pulse is incident on the substrate. More importantly, the change in the damage center is different in these two cases. In the first case, the STE density becomes larger when the delay time increases, and, thus, the seed electron density for the second pulse becomes larger. The spatial distribution of STE is similar to the Gaussian distribution, which is large at the center but small at the edge. The range of CB free electron density, therefore, becomes larger, which is from the edge of the first laser beam toward the laser beam center. This expansion of range leads to the result that the damage center moves toward the laser beam center of the first pulse. But the result in the second case is contrary to the first case. This is because of the decay of STE. In the second case where delay $\Delta t > 400$ fs, STE becomes the only source for the seed electrons and the density of STE decreases when the delay time is longer. Thus, the range of CB free electron density becomes narrowed, which is from the edge of the first beam toward the edge of the second beam leading to a change of damage center toward the edge of the laser beam of the first pulse. Finally, the damage forms at the overlapping area of the two pulses. From this point of view, the change of damage center depends on the STE density when the delay time is longer than the decay time of free electrons, and it is possible to control the damage formation at the overlapping area of two pulses.

Figures 3(a) and 3(b) show the changes in laser damage shape and size measured and simulated at different delay times. The delay time changes from –600 to 600 fs. In Fig. 3(a), there is a significant change in the damage shape from elliptical to "tear-drop" shape at 100 fs and then from the "tear-drop" shape to circle at 200 fs. The same trend also exists in the change of damage diameter as shown in Fig. 3(b). This trend could be explained by the change in the free electron and STE densities at different delay times. As discussed above, the decay of free electrons excited by the first pulse leads to a localization of final free electrons excited by the second pulse in the area of the first pulse. Thus, the elliptical shape of damage changes to the "tear-drop" shape at first and then becomes circular. The damage size is measured along the long axis of the ellipse and thus the change of size follows the same trend. More importantly, the smallest damage size is around 4 μm, which is smaller than the diffraction limit of 20 μm in the optical system of this study. The change in the damage depth at different delay times shares a similar trend to the change of the damage size as shown in Figs. 4(a) and 4(b). This could be explained by the change of free electron density as follows. The free electrons are not only excited by the laser at the surface of the sample but also along the laser propagation direction. The mechanism between free electron and STE occurs at the surface and also along the laser propagation direction. Thus, the phenomena at the surface should also occur along the propagation direction.

V. CONCLUSION

In summary, experiments and simulations of ultrafast laser-induced damage on fused silica by temporally and spatially separated pulses are conducted. The position of damage formation is found to depend on the free-carrier distribution generated by the first pulse. More importantly, the damage center deviates from the center of overlapping area at first and then returns to the center when the delay time is larger than the lifetime of free electrons but shorter than the lifetime of STE. This is due to the change of STE density and provides a possibility that the damage can be controlled to form at the overlapping area with a damage size smaller than the diffraction limit. In addition, the changes in the damage morphology at the surface and depth along the laser beam propagation direction share a similar trend, and the decay of free electrons, which are originally produced by the first pulse, leads to a sharp change in the shape, size, and depth when the delay time is shorter than the lifetime of free electrons. A simple but effective model including the STE density rate equation is developed to simulate the free-carrier density during the damage formation.

ACKNOWLEDGMENT

This paper is based upon work supported by the National Science Foundation (NSF) under Grant No. 1846671.

REFERENCES

[1]R. R. Gattass and E. Mazur, "Femtosecond laser micromachining in transparent materials," Nat. Photonics **2**, 219–225 (2008).
[2]D. Du, X. Liu, G. Korn, J. Squier, and G. Mourou, "Laser-induced breakdown by impact ionization in SiO_2 with pulse widths from 7 ns to 150 fs," Appl. Phys. Lett. **64**, 3071–3073 (1994).
[3]P. P. Pronko, S. K. Dutta, J. Squier, J. V. Rudd, D. Du, and G. Mourou, "Machining of sub-micron holes using a femtosecond laser at 800 nm," Opt. Commun. **114**, 106–110 (1995).
[4]A. Rahaman, A. Kar, and X. Yu, "Thermal effects of ultrafast laser interaction with polypropylene," Opt. Express **27**, 5764–5783 (2019).
[5]B. C. Stuart, M. D. Feit, S. Herman, A. M. Rubenchik, B. W. Shore, and M. D. Perry, "Nanosecond-to-femtosecond laser-induced breakdown in dielectrics," Phys. Rev. B **53**, 1749 (1996).
[6]B. C. Stuart, M. D. Feit, A. M. Rubenchik, B. W. Shore, and M. D. Perry, "Laser-induced damage in dielectrics with nanosecond to subpicosecond pulses," Phys. Rev. Lett. **74**, 2248 (1995).
[7]B. C. Stuart, M. D. Feit, S. Herman, A. M. Rubenchik, B. W. Shore, and M. D. Perry, "Optical ablation by high-power short-pulse lasers," J. Opt. Soc. Am. B **13**, 459–468 (1996).
[8]M. Li, S. Menon, J. P. Nibarger, and G. N. Gibson, "Ultrafast electron dynamics in femtosecond optical breakdown of dielectrics," Phys. Rev. Lett. **82**, 2394 (1999).
[9]L. Sudrie, A. Couairon, M. Franco, B. Lamouroux, B. Prade, S. Tzortzakis, and A. Mysyrowicz, "Femtosecond laser-induced damage and filamentary propagation in fused silica," Phys. Rev. Lett. **89**, 186601 (2002).
[10]A. Q. Wu, I. H. Chowdhury, and X. Xu, "Femtosecond laser absorption in fused silica: Numerical and experimental investigation," Phys. Rev. B **72**, 085128 (2005).
[11]A. P. Joglekar, H. H. Liu, E. Meyhöfer, G. Mourou, and A. J. Hunt, "Optics at critical intensity: Applications to nanomorphing," Proc. Nat. Acad. Sci. U.S.A. **101**, 5856–5861 (2004).
[12]V. V. Temnov, K. Sokolowski-Tinten, P. Zhou, A. El-Khamhawy, and D. Von Der Linde, "Multiphoton ionization in dielectrics: comparison of circular and linear polarization," Phys. Rev. Lett. **97**, 237403 (2006).
[13]L. Englert, B. Rethfeld, L. Haag, M. Wollenhaupt, C. Sarpe-Tudoran, and T. Baumert, "Control of ionization processes in high band gap materials via tailored femtosecond pulses," Opt. Express **15**, 17855–17862 (2007).

[14]X. Yu, Q. Bian, Z. Chang, P. B. Corkum, and S. Lei, "Femtosecond laser nanomachining initiated by ultraviolet multiphoton ionization," Opt. Express **21**, 24185–24190 (2013).
[15]D. Grojo, M. Gertsvolf, S. Lei, T. Barillot, D. M. Rayner, and P. B. Corkum, "Exciton-seeded multiphoton ionization in bulk SiO_2," Phys. Rev. B **81**, 212301 (2010).
[16]X. Yu, Q. Bian, B. Zhao, Z. Chang, P. B. Corkum, and S. Lei, "Near-infrared femtosecond laser machining initiated by ultraviolet multiphoton ionization," Appl. Phys. Lett. **102**, 101111 (2013).
[17]X. Yu, Z. Chang, P. B. Corkum, and S. Lei, "Fabricating nanostructures on fused silica using femtosecond infrared pulses combined with sub-nanojoule ultraviolet pulses," Opt. Lett. **39**, 5638–5640 (2014).